npj | materials degradation

Article

Published in partnership with CSCP and USTB

https://doi.org/10.1038/s41529-024-00451-z

The effect of topological design on the degradation behavior of additively manufactured porous zinc alloy

Yixuan Shi[1,2,4], Wei Xu[3,4], Haodong Che[1], Shangyan Zhao[1], Weiwei Chang[1], Xuan Li[1], Yuchen Lu[1], Chenran Xue[1], Dawei Zhang[1,2] ✉, Lu-Ning Wang[1,2] ✉ & Yageng Li[1,2] ✉

The advent of additively manufactured biodegradable porous metals presents a transformative opportunity to meet the criteria of ideal bone substitutes. Precisely tailoring their degradation behavior constitutes a pivotal aspect of this endeavor. In this study, we investigated the effects of topological designs on the degradation profile of laser powder bed fusion (LPBF) Zn scaffolds under dynamic in vitro immersion tests. Specifically, four types of Zn-0.4Mn-0.2Mg scaffolds (beam-based: diamond, face center cubic; surface-based: gyroid, schwarz-P) were designed and fabricated. The degradation mechanism of the scaffolds was comprehensively evaluated using both experimental and simulation methods. The results illuminate the profound impact of structural design on the degradation properties of the Zn alloy scaffolds. The beam-based diamond and face center cubic scaffolds exhibited a degradation rate of 0.08–0.12 mm per year with a relatively uniform degradation mode under dynamic immersion. On the contrary, the surface-based gyroid and Schwarz-P scaffolds demonstrated a notably reduced degradation rate due to lower permeability. This restricted the diffusion of medium ions within the pores, culminating in the accumulation of degradation products and more severe localized degradation. This study underscores the potential of topological design as a compelling strategy for tailoring the degradation profile of additively manufactured biodegradable scaffolds, thereby advancing their suitability as bone substitutes.

One of the most attractive subjects in tissue engineering centers on the development of scaffolds, three-dimensional porous structure that hold immense potential for bone defects repairment[1,2]. An ideal bone scaffold for the treatment of large bony defects should possess several critical attributes: good biocompatibility, an appropriate biodegradation rate, adequate mechanical properties comparable to the anatomical sites[3], and a fully interconnected porous structure. Additionally, it should feature substantial bio-functionalized surface area and a range of permeability values that facilitate cell proliferation and differentiation[4]. Achieving such a combination of characteristics necessitates a meticulous approach to materials selection, elaborate structural design, and the application of advanced manufacturing technique.

Magnesium (Mg) and iron (Fe) have emerged as prominent subjects of study among biodegradable metals, owing to their ability to mitigate chronic local inflammation and physical irritation often associated with bio-inert metals[5–7]. However, Mg alloys face challenges related to rapid degradation and hydrogen evolution, while Fe's limited degradation and undissolvable degradation byproducts are areas of concern[8]. In contrast, zinc (Zn) and its alloys offer an enticing alternative for orthopedic applications[9,10], boasting exceptional mechanical strength[11,12], appropriate degradation rate[13,14], and favorable biocompatibility[15,16]. Moreover, Zn plays an essential role in bone metabolism with a predominantly presence in skeletal muscles and bones (86%) within the human body[17]. Pure Zn scaffolds has been found to exhibited good compatibility and osteogenic ability in both in vitro / in vivo settings[18]. Consequently, the utilization of biodegradable Zn has gained significant traction in the fabrication of scaffolds for the treatment of bone defects.

The advancement of additive manufacturing (AM) techniques provides unprecedented opportunities for crafting patient-specific implants

[1]Beijing Advanced Innovation Center for Materials Genome Engineering, School of Materials Science and Engineering, University of Science and Technology Beijing, Beijing 100083, China. [2]Institute of Materials Intelligent Technology, Liaoning Academy of Materials, Shenyang 110004, China. [3]National Engineering Research Center for Advanced Rolling and Intelligent Manufacturing, Institute of Engineering Technology, University of Science and Technology Beijing, Beijing 100083, China. [4]These authors contributed equally: Yixuan Shi, Wei Xu. ✉e-mail: dzhang@ustb.edu.cn; luning.wang@ustb.edu.cn; yagengli@ustb.edu.cn

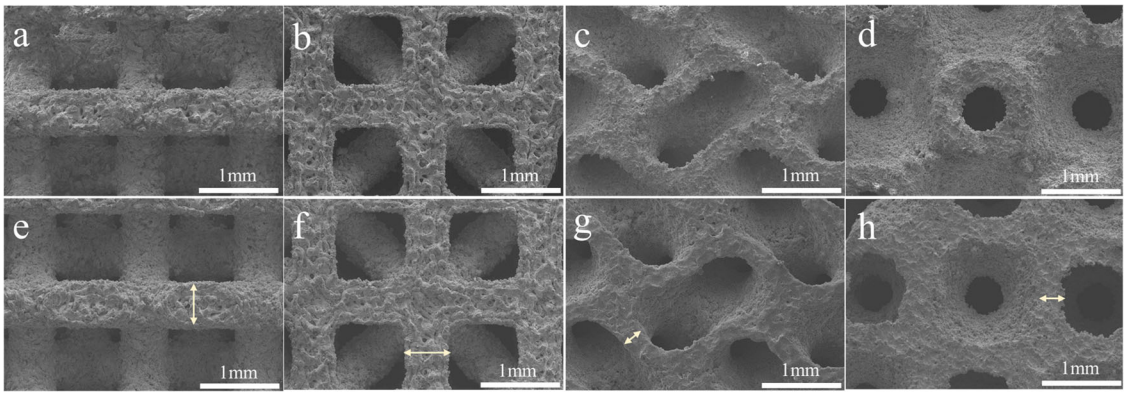

Fig. 1 | Surface morphologies of AM porous Zn alloy. a–d strut morphologies of the as-built (**a**) D, (**b**) F, (**c**) G, (**d**) P specimens, and (**e**, **f**) strut morphologies of the as-polished (**e**) D, (**f**) F, (**g**) G, (**h**) P specimens. (arrows: width of struts).

tailored to precise geometries and mechanical specifications[19,20]. So far, laser powder bed fusion (LPBF) has emerged as a widely adopted method for fabricating metallic components, including biodegradable metals[21,22]. The micro-architected structure of biodegradable Zn or Mg scaffolds could be precisely controlled through LPBF[23]. While previous studies have emphasized the importance of customized geometry, it is noteworthy that optimal degradation rates for bone scaffolds may vary depending on specific bone defect scenarios[4,24–26]. Unlike bulk biodegradable metal, increased surface area of the pores structures resulted in an accelerated degradation rate of the scaffolds[27]. The cellular responses might be impaired due to the excessive release of Zn ions and elevated local pH values[6]. Therefore, a thorough investigation of degradation mechanisms and precise control of the degradation behavior of AM porous Zn alloys is imperative. Notably, Li et al.[28] demonstrated that different topological design can result in up to 3-fold change in permeability and up to 1.5-fold change in biodegradation rate among the AM porous pure Zn. Wang et al.[3] manufactured the Mg scaffolds based on three types of architectures with the same porosity, revealing that the Gyorid scaffold exhibited the lowest structural loss and a relatively uniform degradation mode compared to the diamond and biomimetic unit cell architectures. Nevertheless, to date, the degradation mechanisms of biodegradable metallic scaffolds remain a subject of ongoing investigation.

In the realm of AM bone scaffold design, two primary categories of unit cells exist: beam-based and sheet-based structures[6]. From the perspective of mechanical property, beam-based unit cells can be categorized as either bending or stretching dominated types. Among these, bending-dominated cells exhibit superior energy absorption capabilities, whereas stretching-dominated cells demonstrate higher strength characteristics. Sheet-based structures commonly manifest as minimal surface configurations, known for their proven benefits in fostering cell adhesion and proliferation. Therefore, the exploration of degradation mechanism for AM Zn scaffolds should consider various typical unit cells.

In this study, we employed LPBF to fabricate Zn alloy scaffolds, utilizing four distinct unit cell designs including diamond (D), face center cubic (F), Gyroid (G), and schwarz-P (P). Subsequently, we conducted comprehensive evaluations of their degradation profile and electrochemical properties in vitro. To gain deeper insights into the degradation mechanisms, we conducted supplementary permeability tests, computational fluid dynamics (CFD) simulations, and scanning electrochemical microscopy (SECM) analysis. Our findings provide compelling evidence that topological design can be used as an effective tool to adjust the degradation behavior of AM Zn scaffolds. With further optimization of the porous structures, AM biodegradable Zn alloy scaffolds hold great potential for precise treatment of bone defects in future applications.

Results

Morphological characteristics of the AM porous Zn alloy

According to the SEM images, the surfaces morphology of the as-polished Zn-Mn-Mg scaffolds appeared to be smooth than as-built scaffolds, with clearly discernible porous structures for both unit cells (Fig. 1a–h). There were less un-melted powders for all the scaffolds after polishing. The thickness of the struts or sheets in the scaffolds were consistent with the design, as confirmed by the SEM analysis (Table 1).

In vitro biodegradation behavior

According to the visual inspection, a progressive formation of white particles was observed on the top of the scaffolds from day 3 to day 14, corresponding to the inlet of the SBF flow (Fig. 2a). Among the four design groups, the G and P structures appeared to generate a great number of biodegradation products compared to the D and F ones. For both unit cell, the degradation products were featured with spherical morphology at the edge of the scaffolds (Fig. 2b), while presenting schistose shape within the pores (Fig. 2c). EDS analysis indicated that the degradation products mainly contained Ca, P, O, Mn, Mg, and Zn. Notably, the spherical products had higher Ca, P and O contents compared to the schistose ones. XRD analysis (Fig. 2d) revealed that, the biodegradation products encompassed zinc oxide (ZnO), zinc chloride ($ZnCl_2$), simonkolleite ($Zn_5(OH)_8Cl_2{\cdot}H_2O$), scholzite ($CaZn_2(PO_4)_2{\cdot}2H_2O$), and hydrated zinc phosphate ($Zn_3(PO_4)_2{\cdot}H_2O$). Furthermore, the total spectrum of XPS results confirmed the presence of Zn, Ca, O, C, P, Mg, Mn, and Cl (Fig. 2e). According to the high-resolution XPS spectra, the peaks at 1022.3 eV and 1021.5 eV could be attributed to the formation of $Zn(OH)_2/Zn_3(PO_4)_2$ and $ZnO/ZnCl_2$, respectively (Fig. 2f)[29]. The Ca 2p 3/2 peak was identified at 347.3 eV(Fig. 2g), while P 2p peaks were fitted with two signals at 133.9 and 132.9 eV which might be associated with the formation of $Zn_3(PO_4)_2{\cdot}H_2O$ and $CaZn_2(PO_4)_2{\cdot}2H_2O$ (Fig. 2h)[4]. There were no discernible variations in the degradation products among the four different scaffold designs.

After removing the degradation products, distinct degradation profile could be observed on the top surface of all the scaffolds (Fig. 3). The strut or sheet thickness of all the scaffolds decreased from day 3 to day 28 according to the SEM images. The D and F scaffolds displayed a

Table 1 | Structural characteristics of the AM Zn alloy scaffolds

Unit cell	Design thickness (mm)	As-polished thickness (mm)	Design porosity (%)	As-polished Porosity (%)
D	0.55	0.553 ± 0.17	0.704	0.69 ± 0.07
F	0.51	0.518 ± 0.11	0.694	0.68 ± 0.1
G	0.24	0.254 ± 0.04	0.706	0.67 ± 0.14
P	0.32	0.307 ± 0.12	0.692	0.68 ± 0.21

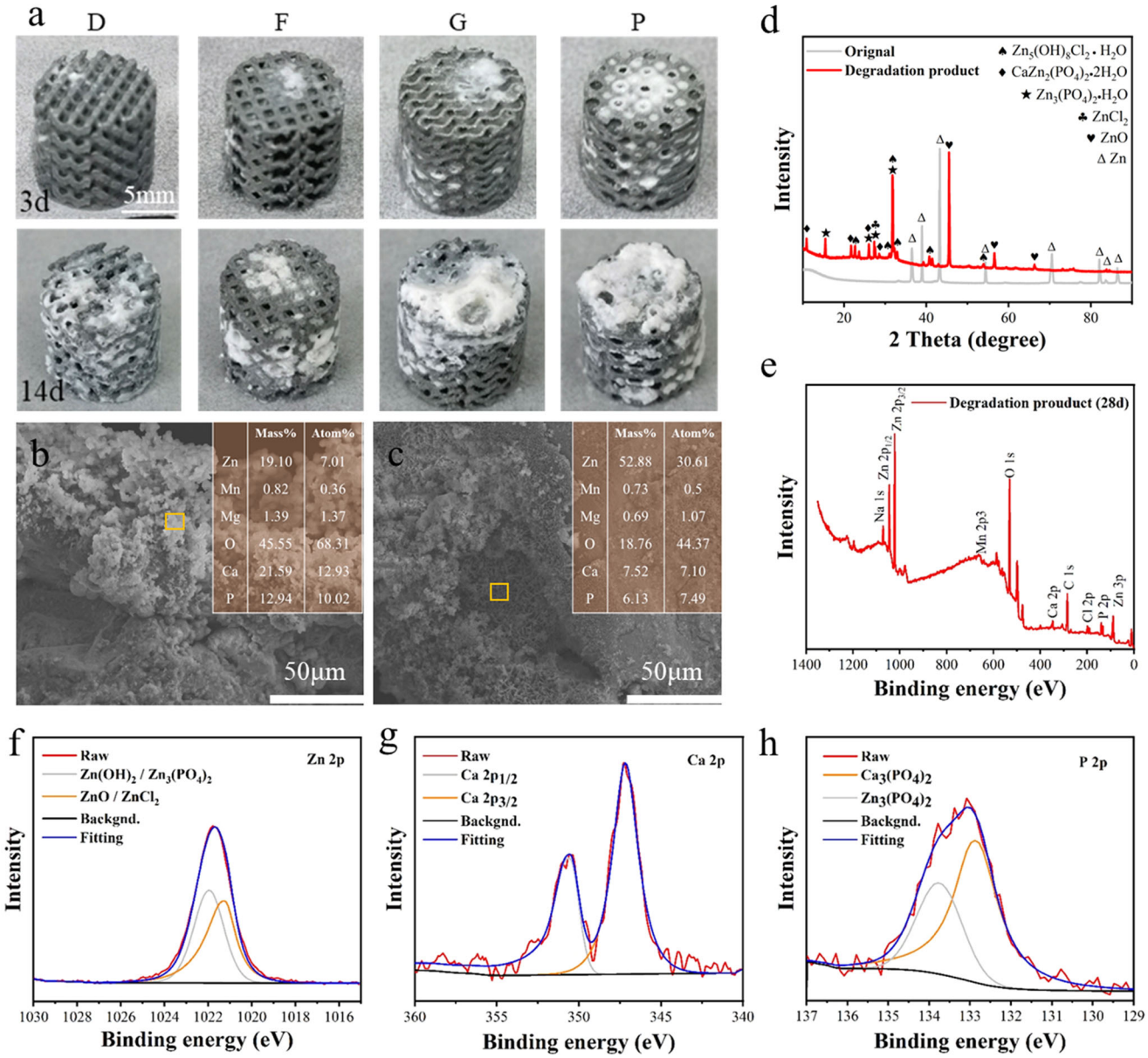

Fig. 2 | Biodegradation products of the AM porous Zn alloy. a visual inspection of the as-degraded scaffolds, (**b**) spherical-like biodegradation products, (**c**) schistose-like biodegradation products, (**d**) XRD analysis, and (**e**–**h**) XPS analysis.

relatively uniform degradation mode, with no significant localized degradation sites observed on the surface (Fig. 3a, b). In contrast, the G scaffold displayed significant degradation after 14 and 28 days, leading to discontinuous appearance on the top (Fig. 3c). Similarly, the P scaffolds experienced localized degradation at the edges and junction of the structures (Fig. 3d).

Throughout the immersion process, the pH value slightly increased from 7.4 to 7.7 for all the Zn scaffolds, with no obvious difference observed among the different designs (Fig. 4a). In terms of the weight loss, the D and F scaffolds consistently exhibited higher value compared to P and G scaffolds at all the immersion time points. Meanwhile, the weight loss of D and F scaffolds nearly doubled at day 28 compare to day 3, whereas the P and G scaffolds remained relatively constant from day 7 to day 28 (Fig. 4b). The degradation rate of all the specimens gradually decreased from 0.2–0.46 mm per year to 0.038–0.124 mm per year from day 3 to day 28. Among these, the D and F scaffolds demonstrated a faster rate of degradation compared to G and P scaffolds at different immersion time. After 28 days, the D and F scaffolds showed more than two times higher degradation rate (0.082–0.124 mm per year) than the G and P designs (0.038–0.041 mm per year). As to the weight loss ratio, the D and F scaffolds exhibited approximately 5% weight loss after 28 days immersion, while the value for G and P scaffolds was around 2% (Fig. 4d).

Reconstructed morphologies of the scaffolds after biodegradation

For a more comprehensive understanding of the degradation mechanism of AM porous Zn alloy, both longitudinal and transversal sections of the scaffolds were scanned using μCT (Fig. 5a–d). After immersion for 28 days, all the four groups remained structural integrity, albeit with some localized degradation, notably more pronounced towards the top compared to the middle of the scaffolds. Moreover, it was observed that local degradation predominantly occurred within the scaffolds rather than at the periphery. In terms of design variations, G and P scaffolds (Fig. 5c, d) exhibited more pronounced localized degradation compared to D and F scaffolds (Fig. 5a, b) at the center.

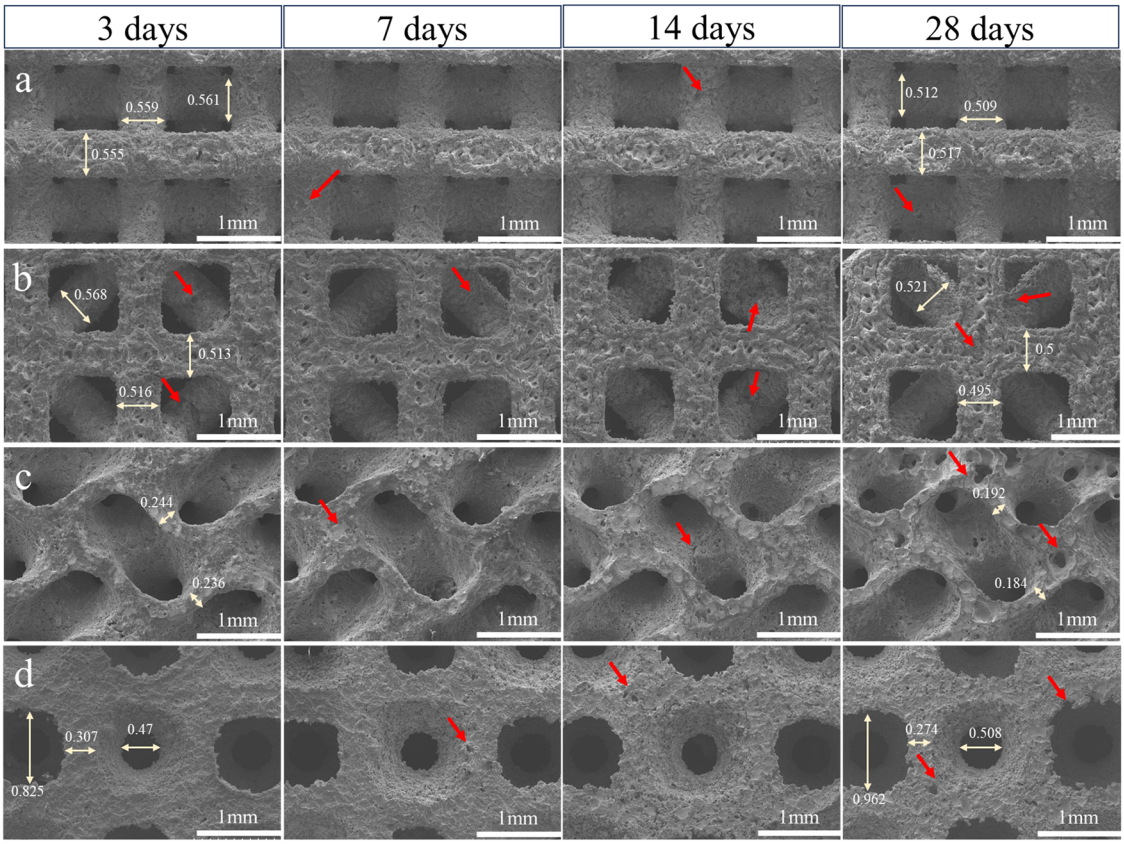

Fig. 3 | Surface morphologies of AM porous Zn alloy after immersion test. Degradation profile of (**a**) D, (**b**) F, (**c**) G, and (**d**) P scaffolds after removal of the degradation products by different immersion time points. (arrows: local degradation).

Electrochemical analysis

The time required to reach a steady-state OCP varied from approximately 800 to 1200 s for different scaffolds among which the P scaffold exhibited more positive OCP compared to the others (Fig. 6a). Electrochemical parameters such as corrosion potential (E_{corr}), corrosion current density (i_{corr}), and cathodic Tafel slope (β_c) were derived from the polarization curves (Fig. 6b and Table 2). When E_{corr} were more or less the same i_{corr} varied with respect to the different structures, during which F and D scaffolds showed almost 6 times higher i_{corr} than P scaffolds. According to the Nyquist plots (Fig. 6c), at the high frequency region, the capacitive loop of P and G scaffolds displayed delayed response characteristics than D and F ones. While at the low frequency region, all the scaffolds exhibited similar mass-transfer behavior. Bode plots (Fig. 6d) showed that at a low frequency region (between 10^{-1} and 10^{1} Hz), the impedance values of the Zn scaffolds declined in the following sequence: P > G > F > D. Moreover, one-time constant could be observed for all the scaffolds in the Bode plots. The P scaffold had a minimum phase angle (~ −8°) corresponded to the higher frequency. According to the data from the fitted equivalent circuit (Table 3) the R_f values of the four scaffolds were lower than that of R_{ct}. For different designs, the P scaffold showed the highest electrochemical resistant with the largest values of R_{ct}.

Microelectrodes characterization

The redox reactions occurring on the surface of the four scaffolds were captured using redox competition modes after 10 min of immersion in SBF (Fig. 7). In the vicinity of a suitably biased conductive or electrochemically active surface, oxidation occurred during scaffold degradation, leading to a decreased concentration of oxygen. The surrounding ones were then attracted to gather at the probe tip, exhibiting a higher feedback current. A higher current indicates the areas with a high rate of oxygen content, while the lower scale colors (magenta and blue) represent relatively passive areas with a low oxygen content. The variations in oxygen concentrations within the pores (Fig. 7a) and on the surface (Fig. 7b) of different scaffolds were monitored over time. Notably, all inner pores areas had lower oxygen concentrations compared to the surface. The order of oxygen concentration of within the pores for different designs was as follows: P < G < F ≤ D (Fig. 7a, b). The electrochemical mapping represented more obvious structural morphology of the P and G scaffolds compared to D and F ones (Fig. 7c–f). In addition, the oxygen current were lower on the P and G scaffolds than the D and F scaffolds.

Velocity distribution and permeability

The CFD analysis revealed that the fluid velocity exhibited non-uniform distribution within the four scaffolds (Fig. 8). Generally, the flow velocity tended to be lower in the vicinity of the beams or surfaces as opposed to the center. In terms of design variations, the P scaffolds demonstrated a higher maximum velocity compared to the others, while the D and F scaffolds exhibited larger areas characterized by high velocities in contrast to the G and P scaffolds.

The permeability values of the scaffolds were measured by using both the simulation results and the drop head method (Table 4). Although the permeability values obtained from the simulations were generally higher than the experiments, they still demonstrated consistent trends among the different designs. Specifically, the permeability of the various Zn scaffolds follows the order: D > F > G > P.

Discussion

Permeability is considered as an important property for both cancellous and cortical bone, which can influence interstitial fluid flow through the bone pores[30–32]. The permeability of cortical bone is less than 1.1×10^{-13} m^2, while trabecular bone shows a wider range of permeability from 0.5×10^{-8} to 5.3×10^{-12} m^2, depending on different

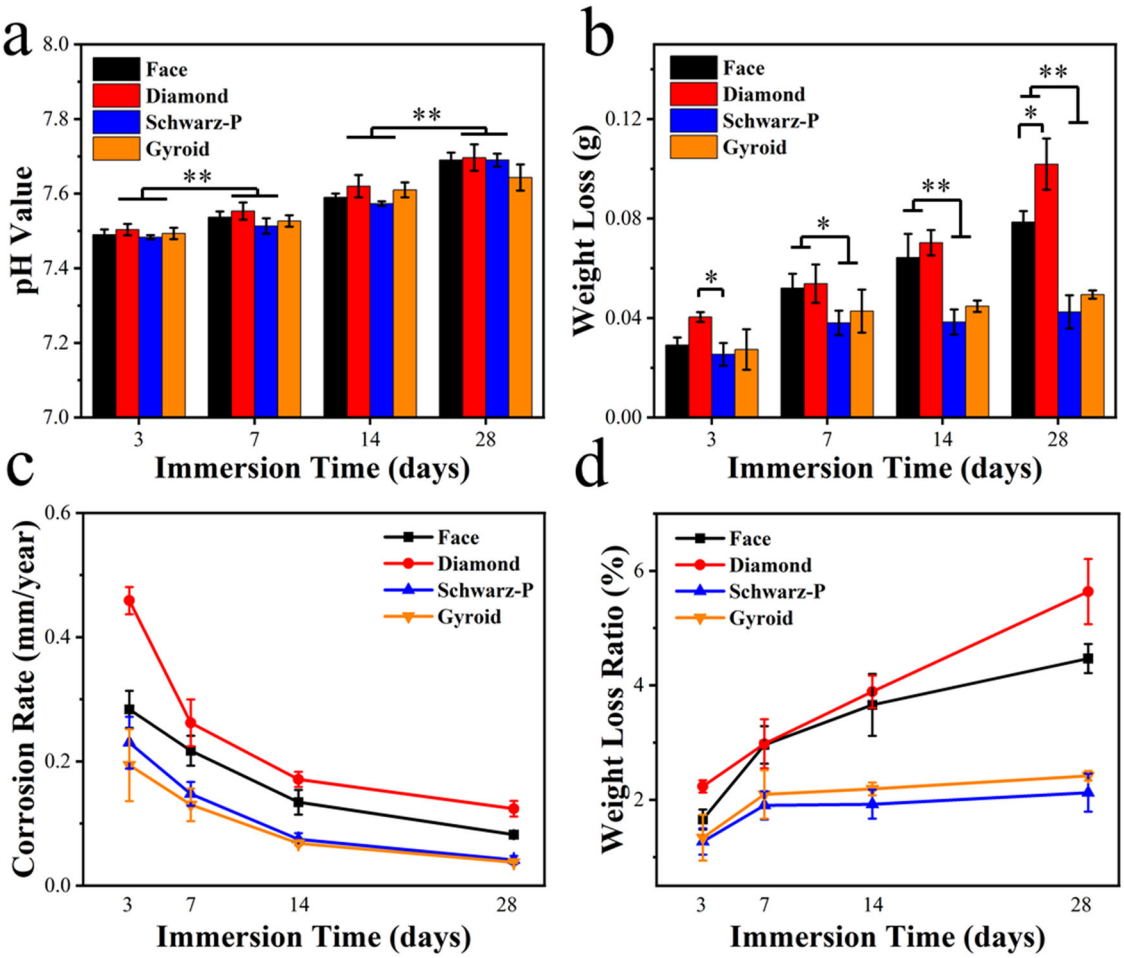

Fig. 4 | Dynamic biodegradation behavior of the AM porous Zn alloy. a pH values, (**b**) weight losses, (**c**) corrosion rates, and (**d**) weight loss ratio at different immersion time points. (*$P < 0.05$, **$P < 0.01$).

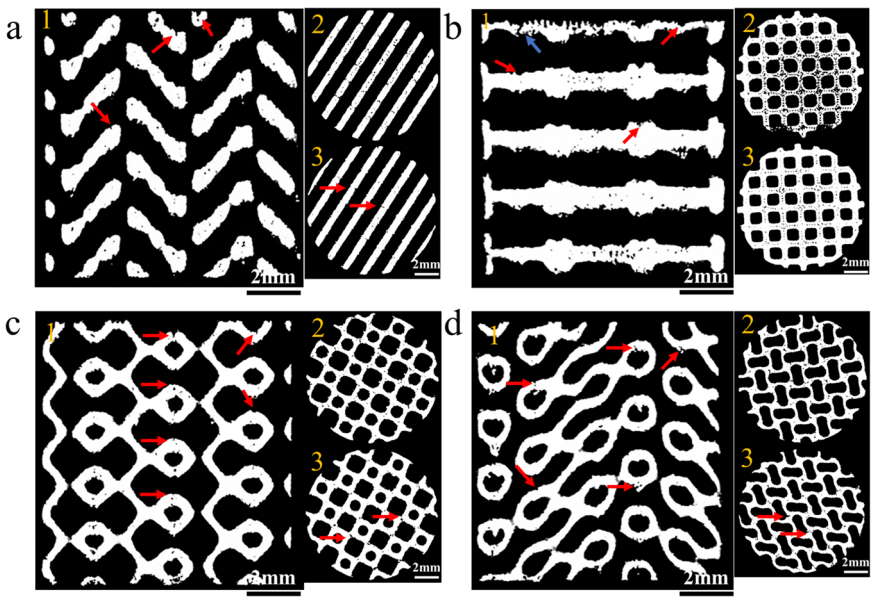

Fig. 5 | Micro-CT analysis of the AM porous Zn alloy after 28 days of biodegradation. a D, (**b**) F, (**c**) G, and (**d**) P. 1: x-z section, 2:x-y section (top), 3:x-y section (middle). (red arrows: local degradation; blue arrow: shear stress effect).

locations[33–36]. Thus, the artificial bone substitutes should have appropriate permeability as well, facilitating the transport of nutrients and oxygen to the cells residing within the scaffolds[37]. Here, AM porous Zn alloy exhibited comparable permeability with human trabecular bone. For example, D and F scaffolds with high permeability are more suitable for the treatment of bone defects from the femur neck, while G and P with lower permeability could be implanted in the mediolateral femoral condyles[30]. Porosity and surface area are two important

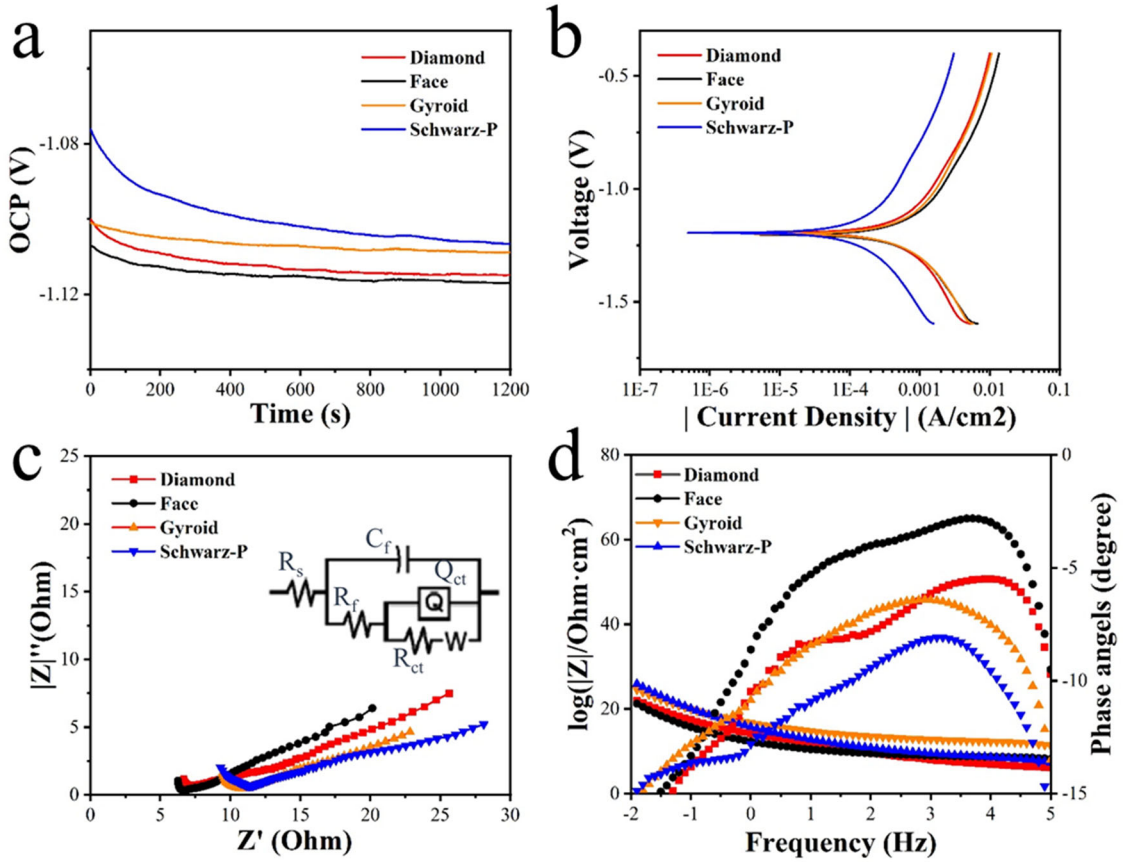

Fig. 6 | Electrochemical characterization of the different AM Zn alloy scaffolds. a OCP, (**b**) PDP, (**c**) Nyquist plots, and (**d**) Bode plots of impedance value | Z| *vs.* frequency and bode plots of phase angle *vs.* frequency.

physical parameters that can affect the permeability of the porous structures[38]. Although the four different designs had the same porosity, G and P scaffolds showed larger surface area than F and P ones (Table 5). Moreover, tortuosity has a direct relationship on the permeability as well, attributed to the shear stress generated by fluid solid coupling that could cause a pressure drop in cancellous structures[33,39].

Table 2 | PDP results for the different AM Zn alloy scaffolds

Cell unit	E_{corr} (V vs. SCE)	i_{corr} (μA cm^{-2}) × 10^{-5}	β_c (mV decade^{-1})
D	−1.19 ± 0.03	66.3 ± 2.7	236 ± 35
F	−1.20 ± 0.02	64.1 ± 3.3	196 ± 62
G	−1.19 ± 0.03	46.7 ± 3.2	149 ± 41
P	−1.19 ± 0.02	15.3 ± 6.8	194 ± 73

Table 3 | EIS fitting results for the different AM Zn alloy scaffolds

Cell unit	R_s (Ω cm^2)	C_f (s^n Ω^{-1} cm^{-2})	R_f (Ω cm^2)	Q_{ct} (s^n Ω^{-1}cm^{-2})	R_{ct} (Ω cm^2)	W (Ω cm^2)	Chi squared
D	10	2.53 × 10^{-8}	5.36	0.051	33.9	0.037	6.05 × 10^{-5}
F	4.02	2.92 × 10^{-7}	2.36	0.14	32.8	0.028	5.40 × 10^{-4}
G	6.66	2.71 × 10^{-7}	2.96	0.13	38.7	0.011	1.24 × 10^{-4}
P	3.2	1.51 × 10^{-7}	3.75	0.08	97	0.03	1.93 × 10^{-4}

Both CFD simulation and falling head experiments demonstrated that the design of unit cell structures could be used to fine-tune the permeability of AM scaffolds. Although some discrepancies existed between the measured and simulated permeability values a strong correlation was evident. This might be attributed to actual surface roughness of the printed scaffold, while the assumed roughness height and roughness constant of scaffold utilized in the simulations were 0 mm and 0.5, respectively. Furthermore, turbulence may have occurred during the experimental measurements, potentially contributing to a deviation from the simulated turbulence coefficient.

Traditionally, the degradation behavior of biodegradable metals has been evaluated under static conditions. However, researchers have increasingly recognized the importance of corrosive medium flow, especially in the context of biodegradable scaffolds[29,40–42]. In the meantime, the ability to control degradation behavior is crucial in the design of a bone substitute. In this study, dynamic immersion with a flow rate of 2 ml·min^{-1} was chosen to mimic the in vivo environment, as 2 ml·min^{-1} closely approximates the fluid flow rate observed in skeletal muscles[43].

Following 28 days of dynamic immersion, white degradation products gradually formed on the surface of all the scaffolds. EDS analysis revealed the presence of Zn, O, Ca, and P elements in the degradation layer. Furthermore, XRD and XPS pattern confirmed the presence of ZnO, $ZnCl_2$, $Zn(OH)_2$, and CaP compound (Fig. 2). Although the local degradations in which Cl^- ions participated were approximately clustered within the pores of scaffolds, the dynamic cycling device allowed for the detection of chloride outside the scaffolds from XRD analysis. Notably, the schistose degradation products contained a higher proportion of Ca and P content than the spherical ones, indicating that the schistose degradation products are more likely to be CaP compounds.

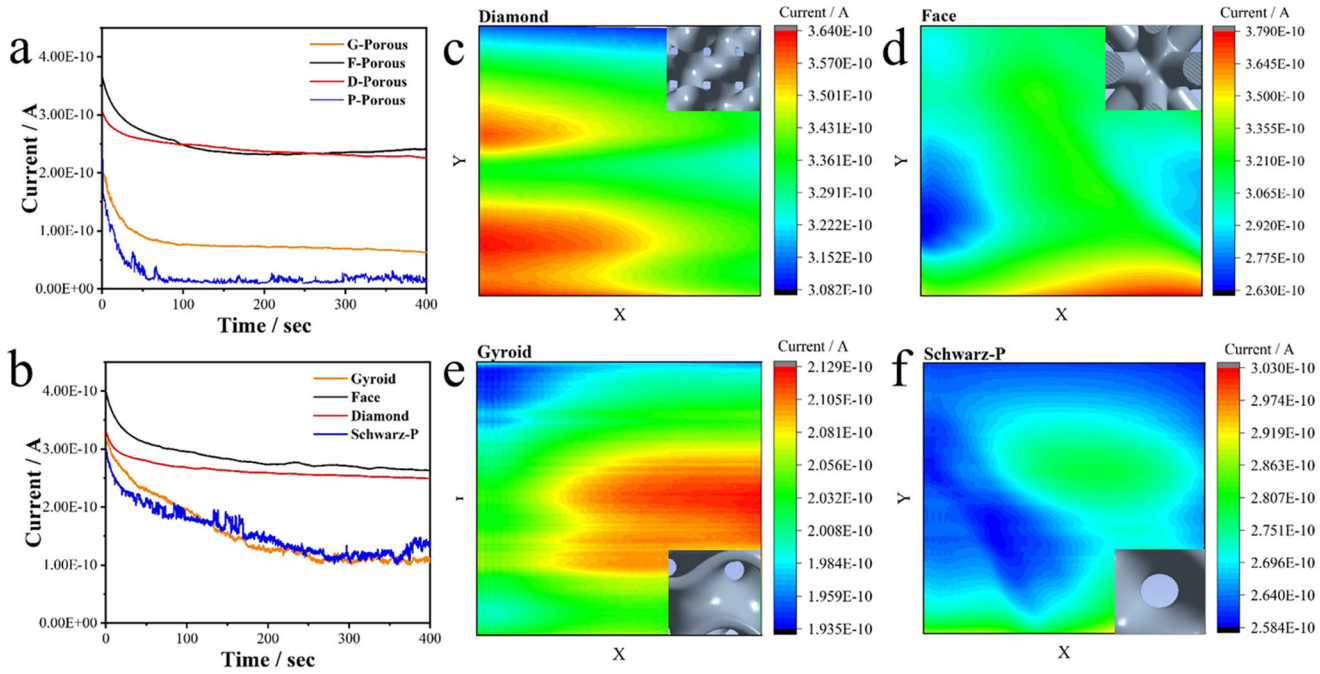

Fig. 7 | SECM images of the AM Zn alloy scaffolds in feedback modes acquired via sensing the oxygen concentration. Oxygen concentration variation (**a**) inside the pores and (**b**) around the surface along with the immersion time, and electrochemical mapping of (**c**) D, (**d**) F, (**e**) G, (**f**) P scaffolds.

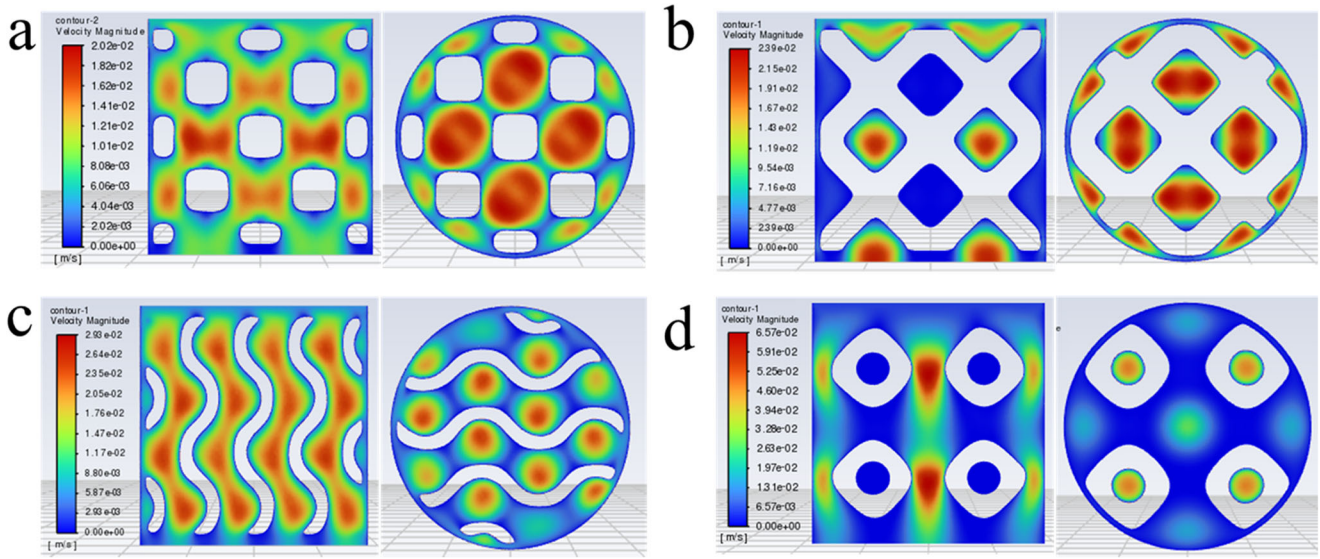

Fig. 8 | Flow velocity distribution within the different AM Zn alloy. a D, (**b**) F, (**c**) G, and (**d**) P scaffolds.

In the case of Zn alloy, the degradation process in SBF can be described by the following reactions:

$$Zn \rightarrow Zn^{2+} + 2e^{-} \quad (1)$$

$$2H_2O + O_2 + 4e^{-} \rightarrow 4OH^{-} \quad (2)$$

$$Zn^{2+} + 2OH^{-} \rightarrow Zn(OH)_2 \quad (3)$$

$$Zn^{2+} + 2OH^{-} \rightarrow ZnO + H_2O \quad (4)$$

Here, Zn^{2+} and OH^{-} are generated from the anodic and cathodic reaction, respectively, leading to the formation of $Zn(OH)_2$, which may later dehydrate into ZnO. When ZnO is present, it could promote the nucleation of CaP compounds. Meanwhile, under weak base conditions, it is beneficial for the formation of CaP compounds such as hydroxyapatite as well[44]. Additionally, the presence of Cl^{-} in the medium may react with the degradation products to form soluble chloride salts through the reactions[4]:

$$6Zn(OH)_2 + Zn^{2+} + 2Cl^{-} \rightarrow 6Zn(OH)_2 \cdot ZnCl_2 \quad (5)$$

$$4ZnO + 4H_2O + Zn^{2+} + 2Cl^{-} \rightarrow 4Zn(OH)_2 \cdot ZnCl_2 \quad (6)$$

Unlike the similar degradation products, the four groups of Zn alloy scaffolds exhibited distinct degradation profile (Figs. 2, 3). The periphery of D and F scaffolds appeared to experience less degradation compared to G and P scaffolds after 14 days of immersion in SBF, as evident from the absence of degradation products (Fig. 2). Interestingly, different from what could be revealed from the visual inspection and SEM images, the

Table 4 | Permeability of the AM Zn alloy scaffolds obtained from the experiments and CFD simulation

Cell unit	Measurement result (10^{-8} m^2)	Simulation ΔP (Pa)	Simulation result (10^{-7} m^2)
D	2.7 ± 0.1	3.7	5.4
F	1.8 ± 0.05	4.2	4.6
G	0.81 ± 0.2	8.3	2.4
P	0.51 ± 0.2	10	2

Table 5 | Surface area of the AM Zn alloy scaffolds

Structure	Design Area (cm^2)
D	15
F	17.5
G	24
P	18.8

degradation rates of D (0.124 mm per year) and F (0.082 mm per year) scaffolds were 2−3 times higher than that of G (0.038 mm per year) and P (0.041 mm per year) scaffolds from the weight loss analysis. According to the micro-CT and SEM results, the D and F scaffolds displayed roughly homogeneous degradation behavior though having the difference between the center and the periphery in the dynamic flow. The sparse local degradation mainly occurred at the connection of the pillars, where shear stress was more concentrated. On the contrary, the G scaffold (Fig. 3c) exhibited obvious uneven biodegradation profile from the interior to exterior zone, as its small pores could be easily blocked by the degradation products. Although the G scaffold underwent more obvious local degradation at the center, the degradation products sealed the pores externally and enhanced the degradation resistance of the whole scaffold under dynamic flow. In addition, due to the low permeability, the biodegradation products could hardly be washed away, resulting in a significant increase in the volume of the biodegradation products for the G and P scaffolds (Fig. 2a). Scaffolds with lower permeability (G and P) were more prone to blockages of the degradation products in the center, leading to non-uniform degradation locally but enhanced degradation resistance in general.

In order to reveal the different corrosion profile from inside to outside of the scaffolds, Micro-CT analysis were conducted on the two typical designs (D and P) before and after 14-days in vitro immersion (Table 6). The outcomes showed that the total volume reduction of the scaffolds was 10.8% and 5.8% for the D and P scaffolds, respectively. Furthermore, we used a circle (5.8 mm diameter) as the region of interest (ROI) to investigate the center and periphery of the scaffolds separately (Supplementary Fig. 1). The volume loss in the central region of the scaffolds D and P were 10.9% and 7.1%, correspondingly. It can be seen that, for the P scaffolds, the differences in degradation rates between the internal and external regions were significant, while the D scaffold exhibited uniform degradation behavior. This is consistent with the degradation profile observed from the SEM images (Fig. 3). During the degradation process, the stagnant flow could be caused with lower permeability inside the scaffold. The diffusion of internal Zn^{2+} ions and external oxygen in the scaffolds could be impeded with the accumulation of the corrosion products. Similar to the crevice-like corrosion, the Cl^- ions could be attracted to the inner part, leading to localized corrosion[45]. Conversely, on the periphery, dynamic flow prevented the adsorption of Cl^- ions on the surface of the corroded layer, thereby ensuring the homogeneity of the biodegradation process. Notably, the top parts of the scaffolds exhibited more serious degradation than the center under the dynamic medium flow (Fig. 5a–d). This can be explained by the fact that within the initial immersion days,

Table 6 | Volume change of the D and P scaffolds before and after 14-days immersion according Micro-CT analysis

Specimen	D (mm^3)	P (mm^3)
As-polished	148	155
As-polished-center	82	85
SBF-14	132	146
SBF-14-center	73	79

the erosion effect of medium flow was greater on the top of the scaffold than that inside the pores.

The electrochemical results indicated the influence of geometric design on the degradation rate of AM Zn scaffolds as well. We found that low-permeability structures exhibited delayed response characteristics in the high-frequency region (Fig. 6c), indicating that the diffusion rate in the P and G scaffolds were lower than the D and F ones. Generally, higher impedance value at low frequency from Bode plots indicates lower degradation rate. The time constant of the phase angle can explain the degree of charge transfer in the high-frequency region[46], which was related to the porous structure. The phase angle values of low-permeability scaffolds could be attributed to the difficulties in the movement of the degradation species for G and P structure. The surface-based scaffolds own lower charge transfer rates and higher degradation resistance, which is consistent with the fitting results (Table 2). The short-term electrochemical data could not represent the long-term degradation behavior after implantation. The degradation products would accumulate on the surface along immersion which can affect the electrochemical properties. However, electrochemical test could be used as a fast-screening method beforehand. We can determine which structure is more prone to degradation from the electrochemical test.

The degradation rate of AM Zn scaffolds is closely related to the diffusion ability of ions[47], which is directly linked to the permeability. At the micro scale, the oxygen concentration in the pores of surface-based scaffolds were significantly lower than that of the D and F ones (Fig. 7a). This discrepancy could be attributed to the low permeability of G and P scaffolds, leading to reduced diffusion rate of oxygen. A schematic diagram has been included to illustrate the diffusion behavior and degradation behavior of the AM D, F, G, and P scaffolds. A decrease in oxygen concentration due to the oxidation reaction. The concentration gradient then drives the surrounding oxygen to approach. Subsequently, the high permeability beam-based scaffolds (Fig. 9a) did not exert a significant impact on ions diffusion. Conversely, ions can only move through specific channels in the face-based scaffolds (Fig. 9b). Of course, the aggregation rate of degradation products is also related to the diffusion rate of ions. The accumulation of degradation products went through four stages (Fig. 9c): initially, oxygen was consumed at the scaffold surface through corrosion reactions, while the slower internal flow rate led to the accumulation of degradation products inside the scaffolds (stage 1); with prolonged immersion time, the accumulation of the degradation products could potentially cause blockage at the top of the scaffolds under the circular SBF (stage 2); as the pores near the top gradually became completely obstructed, degradation products continued to accumulate inside the scaffolds due to the relatively restricted flow (stage 3); oxygen becomes less accessible within the scaffold, hindering the cathodic reaction and promoting the dominance of the anodic reaction, which could result in localized degradation due to the attraction of Cl^- ions within the sealed pores (stage 4)[48].

This mechanism could also explain the more significant difference in the weight loss between different designs after 7 days (Fig. 4). In the early stage of degradation, the P and G had larger surface area while lower permeability compared to the D and F ones. The larger contact area could compensate for the less weight loss caused by lower permeability of P and G design. Along with the accumulation of the degradation products, permeability may play a more important role than the surface area, causing more

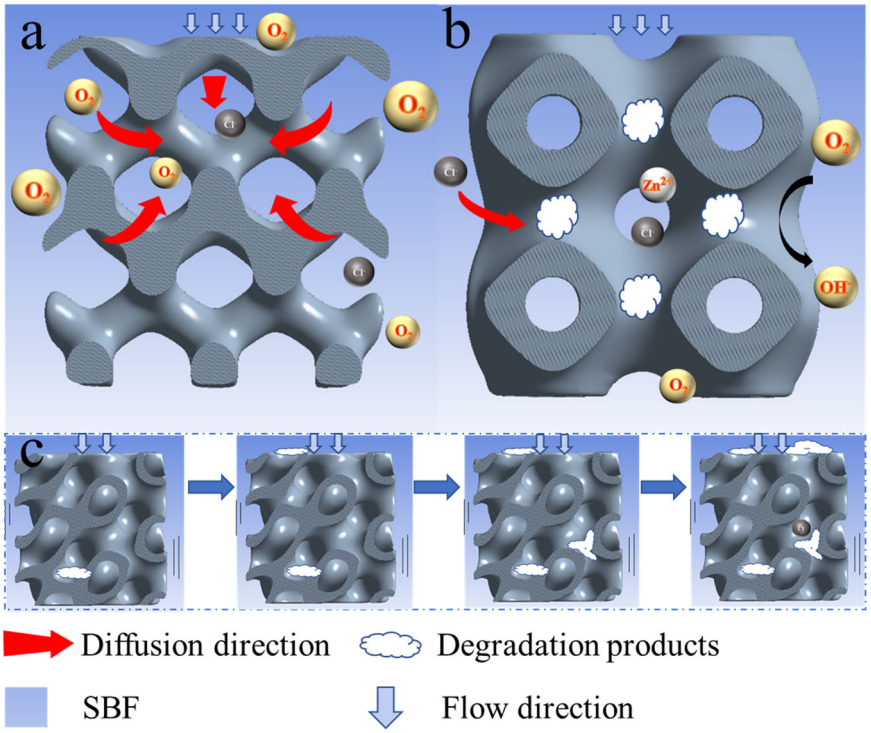

Fig. 9 | Schematic illustration of the ions diffusion and degradation behavior of the AM Zn alloy scaffolds. a D scaffold, (**b**) P scaffold, and (**c**) the degradation products accumulation process.

obvious degradation rate difference between the different designs. The topological design not only changed the diffusion rate of AM Zn scaffolds, it also changed the degradation mechanisms and the formation of degradation products. D and F scaffolds may reduce the probability of localized degradation, thereby reducing implantation issues caused by local failure.

The difference of degradation rates and performances among AM Zn scaffolds underscores the pivotal role of porous structures in controlling the biodegradation profile of porous implants. It is important to note that, in most in vivo cases, Zn alloy scaffolds are expected to maintain mechanical integrity within 3–6 months and gradually degrade over a period of 1–2 years[49,50]. This usually corresponds to the degradation rate of approximately 0.1–0.2 mm per year for the biodegradable bone implants[51]. In this study, the degradation rates of the Zn-Mn-Mg scaffolds ranged from 0.03 to 0.12 mm per year under dynamic conditions, a range that aligns well with the rate of bone regeneration. Furthermore, the degradation profile exhibited consistency between the internal and external location for the beam-based D scaffold. However, within the face-based P scaffold, the degradation rate within the internal region was approximately double that observed in the external region. However, the specific degradation requirements for different defect locations may vary. For instance, complete bone regeneration usually takes 3–12 weeks for the upper limbs, while 12–24 weeks for the lower limbs[18]. Therefore, manipulating the unit cell design showed great potential in aiding us to fine-tune the degradation rate of AM porous Zn for precise bone defect treatment in the future.

In this study, we designed and fabricated four types of Zn-0.4Mn-0.2Mg scaffolds utilizing the LPBF method, based on different unit cells: diamond, face centered cubic, gyroid, and schwarz-P. Afterwards, we systematically assessed the degradation performances of these AM Zn scaffolds through dynamic immersion and electrochemical tests. The G and P (0.082–0.124 mm per year) scaffolds showed slower degradation rates than the D and F ones (0.038–0.041 mm per year), which could be attributed to the lower permeability of surface-based scaffolds. On the contrary, face-based G and P scaffolds exhibited less resistance to localized degradation in comparison to D and F scaffolds, likely due to the limited ion diffusion as observed through SECM and possible vulnerability to Cl^- ion attack. The utilization of topological design offers a long-awaited solution for regulating degradation rates in bone scaffolds without altering porosity. Consequently, AM biodegradable Zn scaffolds hold substantial potential in meeting the requirements for precise treatment of diverse bone defects in the future.

Methods

Scaffold manufacturing

Cylindrical scaffolds (10 mm in height and 10 mm in diameter) were designed based on beam-type (D, F) and surface-type (G, and P) unit cells (unit cell size: 2 mm, strut thickness: 0.2–0.5 mm) (Fig. 10a). The Zn-0.4Mn-0.2Mg scaffolds were fabricated through LPBF (SLM 125 SLM Solution, Germany), equipped with a maximum laser power of 50 W and oxygen levels maintained below 50 ppm within the build chamber. The manufacturing process involved the deposition of a 30 μm thickness powder layer at an energy density of 31.25 $J{\cdot}mm^{-3}$. After printing, wire electrical discharge machining was utilized to separate the specimens from the Zn baseplate. To ensure the removal of any residual powder particles trapped within the pores of the specimens, ultrasonic cleaning with 96% ethanol was conducted for a duration of 15 min. Additionally, the specimens underwent chemical polish in a solution composed of 5% (by volume) hydrochloric acid, 5% nitric acid, and 90% ethanol for 5 min. This was succeeded by another round of ultrasonic cleaning with 96% ethanol to thoroughly rinse away any remaining traces of acids.

Morphological characterization

Micro-computed tomography (μCT) was used to scan the Zn specimens with the following parameters: a tube current of 150 μA, a tube voltage of 120 kV, and a resolution of 5.6 μm, generating a total of 1600 projections. Subsequently, μCT were automatically reconstructed and converted into a series of 2D images using Analyze 11.0 (Perkin Elmer, USA). These 2D images were then exported to FIJI (NIH, USA) for local thresholding. The local thresholding process allowed for accurate segmentation of the Zn specimens, allowing for the comprehensive capture of their morphological characteristics, including shape, size, and distribution.

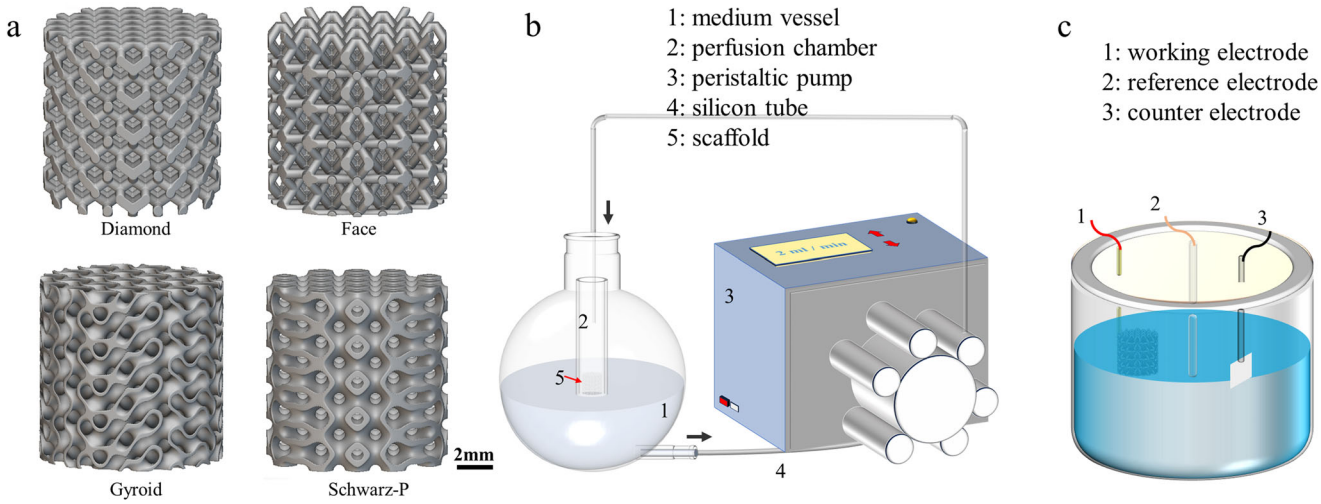

Fig. 10 | Structure design and immersion set-up for AM porous Zn alloy. a D, F, G, and P scaffolds, (**b**) dynamic degradation set-up and (**c**) electrochemical test set-up.

Dynamic immersion tests

Dynamic in vitro immersion tests were performed in simulated body fluid (SBF) at 37 °C for 28 days, utilizing a self-designed bioreactor (Fig. 10b). The SBF was circulated in the bioreactor at a unidirectional flow rate of 2 ml·min^{-1} to mimic the moderate physiological fluid movement in human bone[52]. To closely monitor the progress of biodegradation, pH values of the medium were tracked (accuracy: ± 0.002, Ohaus, USA) at 3, 7, 14, and 28 days.

Morphological and compositional analysis of the biodegradation products was performed using a Scanning Electron Microscope (SEM, Regulus 8100, Japan) in conjunction with an Energy-Dispersive X-ray Spectroscope (EDS). The identification of phases in the biodegradation products was carried out using an X-ray Diffractometer (XRD, Rigaku TTRIII, Japan), operating at 45 kV with a Cu Kα target and a scanning range spanning 10–90° over a 14 min duration. In addition, the surface chemical states of the specimens following biodegradation were analyzed using X-ray Photoelectron Spectroscopy (XPS, Thermo Scientific, K-Alpha, USA). Spectral data were processed and analyzed using Avantage v5.9 software (Thermo Fisher Scientific, USA).

Weight loss was determined by first removing the degradation products with 15% ammonia solution, followed by ultrasonic cleaning in 96% ethanol for 5 min, and subsequently air drying at ambient temperature. The corrosion rate (CR, mm per year) was calculated based on weight loss (W) according to the following equation[53]:

$$CR = k \times \frac{w}{\rho A t} \quad (7)$$

where k is a constant value (8.76×10^4), ρ is the material density, t is immersion time (year), A is sample surface area (Table 5). All the tests were performed in triplicate.

Electrochemical analysis

Electrochemical tests were conducted using an electrochemical workstation (Metrohm AG, Switzerland) with SBF as the electrolyte at a temperature of 37.5 ± 0.5 °C. The AM porous Zn specimens were electrically connected via a copper wire on one side, which was then encapsulated in epoxy resin for insulation. The scaffolds were totally immersed in the SBF during the electrochemical test. Cylindrical surface area (4.71 cm^2) was used as the surface area for different specimens exposed to the electrolyte. A three-electrode electrochemical cell was established with the Zn specimen serving as the working electrode, a platinum mesh acting as the counter electrode, and a saturated calomel electrode utilized as the reference electrode (Fig. 10c). Potentiodynamic polarization (PDP) and electrochemical impedance spectroscopy (EIS) measurements were performed following a 30 min stabilization period after reaching the open circuit potential (OCP). During the PDP measurement, the working electrode was scanned within the voltage range of ±1 V (*versus* OCP) at a scan rate of 0.5 mV·s^{-1}. EIS were performed with 10 mV amplitude across a frequency range spanning from 100 kHz to 10 MHz. The impedance data were analyzed with the Zsimp (AMETEK, USA) and fitted to the equivalent electrical circuits: where R_s represented the solution resistance; R_f and constant phase element C_f were applied to describe the resistance and non-ideal capacitance properties of the biodegradation film, respectively; Q_{ct} represented constant phase angle element, R_{ct} denotes charge transfer resistance and with a Warburg resistance (W) in series. All the tests were performed in triplicates.

Scanning electrochemical microscopy

SECM was employed to provide in situ mapping at different redox states on the specimen surface and inside the pores of the scaffolds[54,55]. A 15 µm platinum (Pt) ultra-micro-electrode (UME) with a resistance greater than 10 ohms (RG > 10) was used as the working electrode. A Pt wire and a Ag/AgCl/KCl (3 M) served as the counter and reference electrodes respectively. The Pt microelectrode tip was positioned to the specimen surface was according to a negative feedback current-distance response by applying + 0.5 V in the ferrocene-methanol mediator. Afterwards, the ferrocene-methanol mediator was replaced by SBF and the tip was set at a constant height of 30 µm from the specimen surface to (prevent touching during movement). The scanning was conducted after 400 s stabilization. The x-y plane was then scanned at the indicated potential for each specimen. In addition, oxygen inside the pores of different Zn alloy scaffolds were detected by Pt microelectrode tip with 1.5 mm depth penetration. All experiments were repeated 3 times.

Computational fluid dynamics analysis

CFD analysis was conduct using the Ansys Fluent™ software (Ansys, USA), to explore the velocity distribution inside the scaffolds and to numerically evaluate the permeability. To streamline the calculation, a scaled-down version of the scaffolds with a diameter of 4 mm and a height of 4 mm were established. The perfusion media, water was modelled as a Newtonian fluid with a dynamic viscosity = 0.001 Pa·s and density = 1000 kg·m^{-3}. A velocity of 0.006 m·s^{-1} was applied to the inlet to ensure that fluid flow remained laminar throughout the scaffold. Generally, the fluid flow is within the laminar range when the Reynolds number is less than 500. The Reynolds number was 5–8 under the simulation velocity, complying with the Darcy's law[43]. An outlet-boundary condition with no constraint was set for outflow.

The pressure drop between the inlet and the outlet was recorded and the permeability was calculated according to Darcy's Law:

$$-\Delta P = \frac{u\mu}{k}$$

where μ is the fluid viscosity, u is the velocity, k is the permeability, ΔP is the fluid averaged pressure.

Permeability

The permeabilities of the specimens were measured utilizing the falling head method[28]. In this procedure, the specimens were placed in a chamber located below a standpipe. The height of the initial and cut-off levels was fixed, and the outflow time was recorded from the moment the water began to fall until it reached the cut-off level. The instantaneous water level was then correlated with the corresponding measured time. The following equation was used to calculate permeability (k):

$$k = \frac{a}{A}\frac{L}{t}Ln\frac{H1}{H2}\frac{\mu}{\rho g} \quad (9)$$

where a and A represent the cross-section areas of the standpipe and specimen, respectively, L denotes the specimen height, $H1$ and $H2$ indicate the momentary levels of water at two different time points, t signifies the interval between these two-time points, μ stands for the dynamic viscosity, and ρ represents the density of water. The tests were performed in triplicate for each of the groups.

Statistical analysis

All experimental data were expressed as the means ± standard deviations. One-way analysis of variance (ANOVA) was used to analyze the statistical significance of the differences between groups. $^{*}P < 0.05$, $^{**}P < 0.01$ was considered statistically significant.

Data availability

All data generated or analysed during this study are included in this published article [and its supplementary information files].

Received: 17 October 2023; Accepted: 15 March 2024;
Published online: 24 April 2024

References

1. Yusop, A. H., Bakir, A. A., Shaharom, N. A., Abdul Kadir, M. R. & Hermawan, H. Porous Biodegradable Metals for Hard Tissue Scaffolds: A Review. *Inter. J. Biomater.* **2012**, 641430 (2012).
2. Zadpoor, A. A. & Malda, J. Additive Manufacturing of Biomaterials, Tissues, and Organs. *Ann. Biomed. Eng.* **45**, 1–11 (2017).
3. Wang, Y., Huang, H., Jia, G., Zeng, H. & Yuan, G. Fatigue and dynamic biodegradation behavior of additively manufactured Mg scaffolds. *Acta Biomater.* **135**, 705–722 (2021).
4. Li, Y. et al. Additively manufactured biodegradable porous zinc. *Acta Biomater.* **101**, 609–623 (2020).
5. Zhu, X. et al. Creation of Bioactive Ceramic Composite Coatings on Zn–Mn–Mg Alloy via Micro-arc Oxidation and Hydrothermal Treatment for Orthopedic Implant Applications. *ACS Appl. Eng. Mater.* **1**, 734–743 (2023).
6. Li, Y., Jahr, H., Zhou, J. & Zadpoor, A. A. Additively manufactured biodegradable porous metals. *Acta Biomater.* **115**, 29–50 (2020).
7. Li, Y. et al. Additively manufactured biodegradable porous iron. *Acta Biomater.* **77**, 380–393 (2018).
8. Kabir, H., Munir, K., Wen, C. & Li, Y. Recent research and progress of biodegradable zinc alloys and composites for biomedical applications: Biomechanical and biocorrosion perspectives. *Bioact. Mater.* **6**, 836–879 (2021).
9. Sun, J. et al. Development of a high-strength Zn-Mn-Mg alloy for ligament reconstruction fixation. *Acta Biomater.* **119**, 485–498 (2021).
10. Shi, Z.-Z., Li, M., Li, X.-M. & Wang, L.-N. Surface-Roughness-Induced Plasticity in a Biodegradable Zn Alloy. *Adv. Mater.* **35**, 2207570 (2022).
11. Yang, H. et al. Alloying design of biodegradable zinc as promising bone implants for load-bearing applications. *Nat. Commun.* **11**, 401 (2020).
12. Guo, P. et al. Ultrafine- and uniform-grained biodegradable Zn-0.5Mn alloy: Grain refinement mechanism, corrosion behavior, and biocompatibility in vivo. *Mat. Sci. Eng.: C* **118**, 111391 (2021).
13. Shi, Y. et al. Corrosion and Biocompatibility of Pure Zn with a Micro-Arc-Oxidized Layer Coated with Calcium Phosphate. *Coatings* **11**, 1425 (2021).
14. Zhao, L. et al. Mechanical properties and in vitro biodegradation of newly developed porous Zn scaffolds for biomedical applications. *Mater. Design* **108**, 136–144 (2016).
15. Shi, Y. et al. A novel MAO-PLA coating on zinc alloy for potential orthopedic implant material. *Mater. Lett.* **317**, 132058 (2022).
16. Wang, X. et al. In vivo study of the efficacy, biosafety, and degradation of a zinc alloy osteosynthesis system. *Acta Biomater.* **92**, 351–361 (2019).
17. Katarivas Levy, G., Goldman, J. & Aghion, E. The Prospects of Zinc as a Structural Material for Biodegradable Implants—A Review Paper. *Metals* **7**, 402 (2017).
18. Xia, D. et al. Additively manufactured pure zinc porous scaffolds for critical-sized bone defects of rabbit femur. *Bioact. Mater.* **19**, 12–23 (2023).
19. Li, Y. et al. Additively manufactured biodegradable porous magnesium. *Acta Biomater.* **67**, 378–392 (2018).
20. Grasso, M., Demir, A. G., Previtali, B. & Colosimo, B. M. In situ monitoring of selective laser melting of zinc powder via infrared imaging of the process plume. *Robot. CIM-INT. Manuf.* **49**, 229–239 (2018).
21. Wei, K. et al. Selective laser melting of Mg-Zn binary alloys: Effects of Zn content on densification behavior, microstructure, and mechanical property. *Mat. Sci. Eng: A* **756**, 226–236 (2019).
22. Zhang, W.-n, Wang, L.-z, Feng, Z.-x & Chen, Y.-m. Research progress on selective laser melting (SLM) of magnesium alloys: A review. *Optik* **207**, 163842 (2020).
23. Guaglione, F., Caprio, L., Previtali, B. & Demir, A. G. Single point exposure LPBF for the production of biodegradable Zn-alloy lattice structures. *Addit. Manuf.* **48**, 102426 (2021).
24. Shi, Y. et al. Surface modification on biodegradable zinc alloys. *J. Mater. Res. Technol.* **25**, 3670–3687 (2023).
25. Bowen, P. K., Drelich, J. & Goldman, J. Zinc Exhibits Ideal Physiological Corrosion Behavior for Bioabsorbable Stents. *Adv. Mater.* **25**, 2577–2582 (2013).
26. Zheng, Y. F., Gu, X. N. & Witte, F. Biodegradable metals. *Mater. Sci. Eng.: R: Rep.* **77**, 1–34 (2014).
27. Liu, Y. et al. Fundamental Theory of Biodegradable Metals—Definition, Criteria, and Design. *Adv. Funct. Mater.* **29**, 1805402 (2019).
28. Li, Y. et al. Additively manufactured functionally graded biodegradable porous zinc. *Biomater. Sci.* **8**, 2404–2419 (2020).
29. Liu, A. et al. Mechanical properties, in vitro biodegradable behavior, biocompatibility and osteogenic ability of additively manufactured Zn-0.8Li-0.1Mg alloy scaffolds. *Biomater. Adv.* **153**, 213571 (2023).
30. Beno, T., Yoon, Y.-J., Cowin, S. C. & Fritton, S. P. Estimation of bone permeability using accurate microstructural measurements. *J. Biomech.* **39**, 2378–2387 (2006).
31. Kohles, S. S. et al. Direct perfusion measurements of cancellous bone anisotropic permeability. *J. Biomech.* **34**, 1197–1202 (2001).
32. Malachanne, E., Dureisseix, D., Cañadas, P. & Jourdan, F. Experimental and numerical identification of cortical bone permeability. *J. Biomech.* **41**, 721–725 (2008).

33. Syahrom, A., Abdul Kadir, M. R., Harun, M. N. & Öchsner, A. Permeability study of cancellous bone and its idealised structures. *Med. Eng. Phys.* **37**, 77–86 (2015).
34. Grimm, M. J. & Williams, J. L. Measurements of permeability in human calcaneal trabecular bone. *J. Biomech.* **30**, 743–745 (1997).
35. Gómez, S., Vlad, M. D., López, J. & Fernández, E. Design and properties of 3D scaffolds for bone tissue engineering. *Acta Biomater* **42**, 341–350 (2016).
36. Foroughi, A. H., Liu, D. & Razavi, M. J. Simultaneous optimization of stiffness, permeability, and surface area in metallic bone scaffolds. *Int. J. Eng. Sci.* **193**, 103961 (2023).
37. Melchels, F. P. W. et al. The influence of the scaffold design on the distribution of adhering cells after perfusion cell seeding. *Biomaterials* **32**, 2878–2884 (2011).
38. Innocentini, M. D. M., Lefebvre, L. P., Meloni, R. V. & Baril, E. Influence of sample thickness and measurement set-up on the experimental evaluation of permeability of metallic foams. *J. Porous Mat.* **17**, 491–499 (2010).
39. Innocentini, M. D. M. et al. Permeability of porous gelcast scaffolds for bone tissue engineering. *J. Porous Mat.* **17**, 615–627 (2010).
40. Shi, Z.-Z., Yu, J., Liu, X.-F. & Wang, L.-N. Fabrication and characterization of novel biodegradable Zn-Mn-Cu alloys. *J. Mater. Sci. Technol.* **34**, 1008–1015 (2018).
41. Zhu, X. et al. Comparison of the in vitro corrosion behavior of biodegradable pure Zn in SBF, 0.9% NaCl, and DMEM. *Mater. Corros.* **72**, 1687–1701 (2021).
42. Pan, K. et al. Facile fabrication of biodegradable endothelium-mimicking coatings on bioabsorbable zinc-alloy stents by one-step electrophoretic deposition. *J. Mater. Chem. B* **10**, 3083–3096 (2022).
43. Zhao, F., Vaughan, T. J. & McNamara, L. M. Multiscale fluid–structure interaction modelling to determine the mechanical stimulation of bone cells in a tissue engineered scaffold. *Biomech. Model. Mechan.* **14**, 231–243 (2015).
44. Yin, Z.-Z. et al. Advances in coatings on biodegradable magnesium alloys. *J. Magnes. Alloy.* **8**, 42–65 (2020).
45. Zong, Y. et al. Comparison of biodegradable behaviors of AZ31 and Mg–Nd–Zn–Zr alloys in Hank's physiological solution. *Mater. Sci. Eng.: B* **177**, 395–401 (2012).
46. Raj, M. A., Revin, S. B. & John, S. A. Selective determination of 3,4-dihydroxyphenylacetic acid in the presence of ascorbic acid using 4-(dimethylamino)pyridine capped gold nanoparticles immobilized on gold electrode. *Colloid. Surface. B* **87**, 353–360 (2011).
47. Gong, K., Wu, M., Liu, X. & Liu, G. Nucleation and propagation of stress corrosion cracks: Modeling by cellular automata and finite element analysis. *Mater. Today Commun.* **33**, 104886 (2022).
48. Qin, Y. et al. Additive manufacturing of Zn-Mg alloy porous scaffolds with enhanced osseointegration: In vitro and in vivo studies. *Acta Biomater* **145**, 403–415 (2022).
49. Zhou, C. et al. Long-term in vivo study of biodegradable Zn-Cu stent: A 2-year implantation evaluation in porcine coronary artery. *Acta Biomater* **97**, 657–670 (2019).
50. Moravej, M. & Mantovani, D. Biodegradable Metals for Cardiovascular Stent Application: Interests and New Opportunities. *Int. J. Mol. Sci.* **12**, 4250–4270 (2011).
51. Chen, Y., Xu, Z., Smith, C. & Sankar, J. Recent advances on the development of magnesium alloys for biodegradable implants. *Acta Biomater.* **10**, 4561–4573 (2014).
52. Duan, Y. R., Zhang, Z. R., Wang, C. Y., Chen, J. Y. & Zhang, X. D. Dynamic study of calcium phosphate formation on porous HA/TCP ceramics. *J. Mater. Sci. Mater. Med.* **16**, 795–801 (2005).
53. NACE A. Standard guide for laboratory immersion corrosion testing of metals. *ASTM Int*, 1–9 (2012).
54. Li, Z. et al. Adaptive bidirectional extracellular electron transfer during accelerated microbiologically influenced corrosion of stainless steel. *Commun. Mater.* **2**, 67 (2021).
55. Pust, S. E., Maier, W. & Wittstock, G. Investigation of Localized Catalytic and Electrocatalytic Processes and Corrosion Reactions with Scanning Electrochemical Microscopy (SECM). *Zeitschrift für Physikalische Chemie* **222**, 1463–1517 (2008).

Acknowledgements

The work was financially supported by supported by the National Natural Science Foundation of China (52201294, 52231010, 52071028), China Postdoctoral Science Foundation (2022M710345), Natural Science Foundation of Beijing (L212014), Fundamental Research Funds for the Central Universities and the Youth Teacher International Exchange & Growth Program (No. QNXM20220022), and Beijing Nova Program (2022 Beijing Nova Program Cross Cooperation Program No. 20220484178).

Author contributions

Y.X.S.: conceptualization, investigation, writing – original draft, writing – review & editing, visualization. W.X.: investigation, writing – review & editing, visualization. #These authors contributed equally to this work. H.D.C.: investigation, methodology. S.Y.Z.: investigation, visualization. W.W.C.: investigation, visualization. X.L.: investigation, visualization. Y.C.L.: investigation, visualization. C.R.X.: investigation, visualization. D.W.Z.: resources, conceptualization, visualization, guidance/mentorship. L.N.W.: resources, conceptualization, visualization, guidance/mentorship. Y.G.L.: resources, guidance/mentorship, writing – review & editing.

Competing interests

The authors declare no competing interests.

Additional information

Supplementary information The online version contains supplementary material available at https://doi.org/10.1038/s41529-024-00451-z.

Correspondence and requests for materials should be addressed to Dawei Zhang, Lu-Ning Wang or Yageng Li.